

Nanoscale

Accepted Manuscript



This is an *Accepted Manuscript*, which has been through the Royal Society of Chemistry peer review process and has been accepted for publication.

Accepted Manuscripts are published online shortly after acceptance, before technical editing, formatting and proof reading. Using this free service, authors can make their results available to the community, in citable form, before we publish the edited article. We will replace this *Accepted Manuscript* with the edited and formatted *Advance Article* as soon as it is available.

You can find more information about *Accepted Manuscripts* in the [Information for Authors](#).

Please note that technical editing may introduce minor changes to the text and/or graphics, which may alter content. The journal's standard [Terms & Conditions](#) and the [Ethical guidelines](#) still apply. In no event shall the Royal Society of Chemistry be held responsible for any errors or omissions in this *Accepted Manuscript* or any consequences arising from the use of any information it contains.

1
2
3 **In Situ Measurement and Simulation**
4 **of Nano-Magnetite Mobility in Porous**
5 **Media Subject to Transient Salinity**
6

7
8 *Matthew Becker,^a Yonggang Wang,^a Jeffrey Paulsen,^b Yi-Qiao Song,^b*
9 *Linda M. Abriola^a and Kurt D. Pennell^{*,a}*
10

11 ^aDepartment of Civil and Environmental Engineering, Tufts University, 200 College Avenue,
12 Medford, Massachusetts 02155, United States
13

14 ^bSchlumberger-Doll Research Center, 1 Hampshire St, Cambridge, MA 02139, United States

15
16 *Corresponding Author: Kurt D. Pennell

17 Tel: 617-627-3211

18 Fax: 617-627-3994

19 Email: Kurt.Pennell@tufts.edu
20

21
22 For submission to:

23 *Nanoscale*

24 *Original Submission: September 2, 2014*

25 *Revised Submission: October 26, 2014*
26

1 Abstract

2 Nanotechnologies have been proposed for a variety of environmental applications, including
3 subsurface characterization, enhanced oil recovery, and in situ contaminant remediation. For
4 such applications, quantitative predictive models will be of great utility for system design and
5 implementation. Electrolyte chemistry, which can vary substantially within subsurface pore
6 waters, has been shown to strongly influence nanoparticle aggregation and deposition in porous
7 media. Thus, it is essential that mathematical models be capable of tracking changes in
8 electrolyte chemistry and predicting its influence on nanoparticle mobility. In this work, a
9 modified version of a multi-dimensional multispecies transport simulator (SEAWAT) was
10 employed to model nanoparticle transport under transient electrolyte conditions. The modeling
11 effort was supported by experimental measurements of paramagnetic magnetite (Fe_3O_4)
12 nanoparticle, coated with polyacrylamide-methylpropane sulfonic acid – lauryl acrylate (nMag-
13 PAMPS), mobility in columns packed with 40-50 mesh Ottawa sand. Column effluent analyses
14 and magnetic resonance imaging (MRI) were used to quantify nanoparticle breakthrough and in
15 situ aqueous phase concentrations, respectively. Experimental observations revealed that
16 introduction of de-ionized water into the brine saturated column (80 g/L NaCl + 20 g/L CaCl_2)
17 promoted release and remobilization of deposited nanoparticles along a diagonal front,
18 coincident with the variable density flow field. This behavior was accurately captured by the
19 simulation results, which indicated that a two-site deposition-release model provided the best fit
20 to experimental observations, suggesting that heterogeneous nanoparticle-surface interactions
21 governed nanoparticle attachment. These findings illustrate the importance of accounting for
22 both physical and chemical processes associated with changes in electrolyte chemistry when
23 predicting nanoparticle transport behavior in subsurface formations.

1. Introduction

Engineered nanomaterials are currently being evaluated for their potential to improve subsurface applications including oil reservoir characterization,¹⁻⁴ carbon sequestration, enhanced oil recovery,⁵⁻⁸ and groundwater remediation.^{9, 10} The proposed applications rely on the ability to engineer nanoparticles to perform certain tasks within the subsurface environment, including transport to a targeted zone, association with a specific interface, and/or completion of a specific activity or process at that interface.¹⁰ However, performance of these functions is strongly dependent upon particle-particle and particle-surface interaction energies, and as a consequence, the chemistry of the pore water (e.g., ionic strength, pH, concentration of surface-active agents).¹⁰⁻¹³ Since nanoparticle mobility in the subsurface will be a critical process in these applications, the ability to accurately simulate the effects of transient aqueous chemistry on nanoparticle transport behavior is essential for proper delivery system design and deployment (or implementation).

Prior studies have demonstrated that the electrolyte chemistry of nanoparticle suspensions strongly influences their aggregation and deposition potential in porous media.¹⁴ An increase in ionic strength acts to suppress the electrical double layer surrounding a nanoparticle, which decreases the electrostatic repulsion between the nanoparticle and the solid phase surfaces.¹⁵ The response to such a change in solution chemistry is often reflected in macroscale nanoparticle transport behavior, where increasing ionic strength promotes particle-particle aggregation and particle deposition.¹⁶ These effects have been reported for a variety of nanoparticle types, including fullerenes,¹⁷ iron,^{18, 19} titanium dioxide,²⁰⁻²³ silver,²⁴ quantum dots,²⁵ and others.²⁶⁻²⁸ Adding to this complexity, nanoparticles that are introduced into a subsurface formation will be exposed to a variety of dissolved compounds in the interstitial pore water. For example, the

1 presence of divalent cations may also promote aggregation and deposition by bridging
2 complexation,^{24, 29, 30} which could lead to variable interaction energies between particles and
3 surfaces. Despite these potential complexities, most nanoparticle transport studies conducted to
4 date consider nanoparticle deposition to the solid phase as a single-site process and neglect the
5 heterogeneous interaction energies that could be experienced by nanoparticles in natural porous
6 media.

7 Many subsurface formations can experience transient salinity conditions that lead to
8 altered fluid flow behavior.³¹ For example, nanotechnologies have been proposed for use in oil
9 reservoir characterization and enhanced oil recovery.^{2, 5, 7, 32, 33} A fundamental challenge in these
10 applications is the effect of the high salinity reservoir environment (>1 M) on nanoparticle
11 suspension stability.³⁴ While a number of experimental investigations have focused on
12 increasing nanoparticle suspension stability in such harsh pore waters,³⁴⁻³⁶ studies have yet to
13 evaluate the coupled effects of transient electrolyte conditions on variable density fluid flow and
14 nanoparticle transport in the subsurface.

15 Most macroscale mathematical models designed to simulate nanoparticle transport in
16 porous media employ modifications of clean-bed colloid filtration theory.³⁷ For example, a
17 modified filtration theory (MFT) model, which incorporates a limiting retention capacity term
18 (S_{max}), has been successfully used to simulate nanoparticle attachment behavior in a range of
19 soils and aquifer materials, including those subject to transient solution chemistry.³⁸⁻⁴² The
20 deposition behavior of nanoparticles, however, is much better understood than nanoparticle
21 release, in part because irreversible attachment (*i.e.*, no observable detachment) is typically
22 observed under relevant environmental conditions, especially in systems containing divalent
23 cations.^{29, 43} In addition, nanoparticle detachment and re-entrainment in flowing pore water (*i.e.*,

1 release) may strongly depend on transient hydrodynamic and thermodynamic system
2 characteristics,^{44, 45} and may alter the retention capacity of the system.⁴⁶ A few studies have
3 modeled reversible attachment by identifying a releasable fraction of nanoparticles, a system-
4 specific parameter related to the interaction energies between particles and surfaces.^{29, 38, 47}
5 Although these models provide useful information regarding the relative populations of
6 releasable and non-releasable particles in a particular system, they only account for variability in
7 the detachment process, not in the attachment process. In addition, these studies only considered
8 relatively minor variations in ionic strength in freshwater aquifer formations, and thus, do not
9 account for the potential effects of solution density contrasts on flow in estuarine aquifers or oil
10 reservoirs. To our knowledge, no mathematical modeling studies have addressed the coupled
11 influence of transient electrolyte chemistry on nanoparticle attachment-detachment kinetics and
12 flow behavior.

13 The objective of this study was to quantify the coupled physical and chemical effects
14 created by a transient salinity environment on the release behavior of polymer-coated magnetite
15 nanoparticles (nMag) in water-saturated quartz sand. Two column studies were performed; the
16 first was designed to measure the effluent concentration of nMag during transport and release,
17 while the second was designed to obtain *in situ* images of nMag transport behavior using
18 magnetic resonance imaging (MRI).⁴⁸ The initial phases of the nMag transport studies were
19 performed under brine conditions, followed by the introduction of de-ionized (DI) water to
20 explore the release of deposited nanoparticles. The coupled effects of variable density flow and
21 transient ionic strength on nMag release were modeled by modifying an existing variable density
22 groundwater flow simulator to include nMag transport, deposition, and fractional release using

1 an MFT-based approach. To quantify the deposition and release kinetics observed in the column
2 experiments, the model was fit to column effluent data, and further validated using MRI results.

3 **2. Experimental Methods**

4 **2.1 Column Experiments:** Magnetite nanoparticles (nMag, Fe₃O₄), coated with polyacrylamido-
5 methylpropane sulfonic acid-lauryl acrylate (nMag-PAMPS), were utilized in this study based on
6 their propensity to remain stable at high salinity. Details of the synthesis of these particles are
7 presented by Colvin and Zhu.^{4,34} Two replicate column experiments were conducted following
8 methods described in previous studies.^{39,49} Briefly, for both nanoparticle transport experiments
9 (nMag-eff and nMag-MRI), borosilicate glass columns (2.5 cm i.d. × 10 cm length) were dry
10 packed with 40-50 mesh Ottawa sand (U.S. Silica, Berkeley Springs, WV). To ensure complete
11 saturation, the packed columns were purged with CO₂ gas and flushed with at least 10 pore
12 volumes (PVs) of American Petroleum Institute (API) brine solution (8 wt% NaCl, 80 g/L and 2
13 wt% CaCl₂) at pH 7, designed to mimic oil reservoir salinity.³⁴ A pulse (ca. 1.3 PVs) of aqueous
14 nMag suspension (30 mg/L as Fe) was introduced into the brine-saturated column (pH 7),
15 followed by 1.5 PVs of nMag-free brine solution. To investigate the release of attached nMag-
16 PAMPS, the column was then flushed with DI water for 2.6 PV. Due to restricted orientation of
17 the MRI device, the column studies were performed using a horizontal orientation (*i.e.*, flow
18 perpendicular to gravity) at a flow rate of 0.4 mL/min (Darcy velocity of ca. 1.0 m/d). In the
19 first column experiment (nMag-eff), effluent samples were collected continuously to produce an
20 effluent breakthrough curve, represented as the relative effluent concentration versus the number
21 of dimensionless pore volumes injected. In the second column experiment (nMag-MRI), the
22 entire column was located within the MRI device, allowing for the collection of *in situ* images of
23 the flow field following the methods described below. Although the two nMag column

1 experiments were conducted under identical conditions, effluent samples were not collected
2 during the nMag-MRI experiment because of physical restrictions imposed by the magnet.
3 The magnetic imaging device consisted of a wide-bore static field 2T (1H 85 MHz) magnet
4 (Nalorac Cryogenics, Walnut Creek, CA), a Bruker Biospec spectrometer console (Bruker
5 BioSpin, Billerica, MA), and a ParaVision acquisition platform. Prior to use, the MRI system
6 was calibrated using a CuSO₄-doped agar. The brine-saturated column was placed into a radio
7 frequency (RF) probe (i.d. = 125 mm) consisting of a birdcage coil tuned to 85 MHz with both
8 cylindrical axes aligned. The probe was placed horizontally in the center homogeneous region of
9 the magnet. Following calibration and setup of the MRI system, the nMag-MRI column was run
10 according to the procedures outlined above. Sagittal (*i.e.*, side view) and axial (*i.e.*, cross-
11 sectional view) magnetic resonance profiles of the spin-spin relaxation time (T_2) and relaxation
12 rate ($R_2 = 1/T_2$) were obtained every 3.5 min using a multiple slice multiple echo (MSME)
13 imaging experiment⁵⁰ with an in-plane resolution of 0.98 mm and slice thickness of 2 mm with
14 an echo time TE = 13 ms and a repetition time TR = 1.5 s. MSME can yield the equivalent
15 NMR signal decay data as the Carr-Purcell-Meiboom-Gill (CPMG) pulse-echo sequence,^{33, 51} but
16 with spatial resolution. A diagram of the column orientation within the MRI device and the
17 resulting image orientations are presented in Figure S1.

18 **2.2 Analytical Methods:** The mean hydrodynamic diameter of the nanoparticles was determined
19 by dynamic light scattering (DLS) using a Zetasizer Nano ZS Analyzer (Malvern Instruments,
20 Southborough, MA), operated in non-invasive back scattering (NIBS[®]) mode at an angle of 173°. To
21 determine nMag-PAMPS concentrations in aqueous samples, elemental Fe present in the
22 nanoparticles was quantified using an Optima 7300 DV inductively coupled plasma – optical
23 emission spectrometer (ICP-OES; Shelton, CT) based upon a five-point calibration curve

1 obtained over a concentration range of 0.5 to 50 mg Fe/L. Solid-phase samples were collected
 2 near the column inlet and prepared for scanning electron microscopy (SEM) imaging by
 3 attaching sands grain onto an aluminum mount stub (Electron Microscopy Sciences) covered
 4 with conductive carbon tape (Electron Microscopy Sciences). The samples were then air-dried
 5 overnight and analyzed using a Zeiss Ultra Plus field emission SEM (Carl Zeiss Microscopy,
 6 LLC, Peabody, MA) with charge compensation operated at 3 kV.

7

8 **3. Mathematical Model Development**

9 **3.1 Coupled Flow and Transport Model:** The horizontal orientation of the experimental
 10 column, required by the MRI apparatus (see Materials and Methods), coupled with the
 11 application of transient brine chemistry floods, created non-uniform, variable density, flow
 12 conditions. To simulate this flow behavior, a variable density aqueous phase flow equation was
 13 employed.⁵²

$$\nabla \cdot \left[\rho \frac{\mu}{\mu_0} \mathbf{K}_0 \left(\nabla h + \frac{\rho - \rho_0}{\rho_0} \nabla z \right) \right] = \rho S_{s,0} \frac{\partial h_0}{\partial t} + \theta_w \frac{\partial \rho}{\partial C} \frac{\partial C}{\partial t} - \rho_s q_s' \quad (1)$$

14 where $S_{s,0}$ is the specific storage coefficient of the porous medium [L^{-1}], h_0 is the potentiometric
 15 head of the reference fluid (de-ionized water) [L], \mathbf{K}_0 is the hydraulic conductivity tensor [$L T^{-1}$],
 16 ρ is fluid density [$M L^{-3}$], μ is fluid viscosity [$M T^{-1} L^{-1}$], ρ_0 and μ_0 are a reference density and
 17 viscosity, respectively, at which fluid and aquifer properties are known, θ_w is the volumetric
 18 water content [-], h is pressure head [L], z is elevation head [L], and $\rho_s q_s'$ is a volumetric flux
 19 source term [$M L^{-3} T^{-1}$] with ρ_s being the density of the source fluid. Note that for constant
 20 density, this equation reduces to the traditional groundwater flow equation.⁵³ To track the

1 influence of brine concentration on fluid density, the spatiotemporal brine concentration profile
 2 was resolved using a traditional component mass balance equation:

$$\frac{\partial(\theta_w C_i)}{\partial t} = \nabla \cdot (\theta \mathbf{D}_i \nabla C_i) - \nabla \cdot (\theta_w v_p C_i) + q_s C_{i,s} + \sum R_n \quad (2)$$

3 Here C_i is the aqueous concentration of constituent i [M L^{-3}], \mathbf{D}_i is the hydrodynamic dispersion
 4 tensor for constituent i [$\text{L}^2 \text{T}$], v_p is the pore-water velocity [L T^{-1}], q_s is a volumetric flow rate
 5 per unit volume of aquifer representing sources and/or sinks which include constituent i [T^{-1}], $C_{i,s}$
 6 is the concentration of the source/sink fluid, and R_n is the n -th reaction which transforms
 7 constituent i . In the case of brine transport, the cation exchange capacity of the sand was
 8 considered negligible, such that $R_n = 0$.

9 A linearized equation of state (3) was then used to represent density, incorporating a
 10 volumetric expansion coefficient, β_c , for salt concentration (4):

$$\rho = \rho_0 \exp[\beta_c (C - C_0)] \approx \rho_0 + \rho_0 \beta_c (C - C_0) \quad (3)$$

$$\beta_c = \frac{1}{\rho_0} \left(\frac{\partial \rho}{\partial C} \right)_{T,P} \quad (4)$$

11 Solution of equations (1) through (4) was implemented using the SEAWAT version 4 software
 12 package, an open-source groundwater flow and transport code developed by the USGS.⁵²
 13 SEAWAT is a modification of the MODFLOW-MT3DMS suite^{54, 55} which is often used to
 14 simulate variable density groundwater flow and transport due to transient concentration (*i.e.*
 15 salt), heat, or pressure, especially in estuarial environments.^{56, 57} The SEAWAT simulator offers
 16 the ability to account for multiple constituents simultaneously, a feature which was utilized in
 17 this study to examine the influence of transient brine concentration on nanoparticle attachment
 18 and detachment behavior. Note that, in this scenario, it was assumed that the dilute

1 concentrations of nMag (< 30 mg/L) would have a negligible influence on the fluid density
2 (<0.01%).

3 **3.2 Nanoparticle Deposition and Release Models:** Nanoparticle transport was calculated using
4 a balance equation of the form (2), with R_n representing the interaction between nanoparticles
5 and the solid surface. To accommodate two types of deposition sites on the solid surface,
6 strongly-held non-releasable (e.g., in the primary energy minimum) and weakly-held releasable
7 (e.g. in the secondary energy minimum) sites, utilization of a commonly employed two-site
8 filtration model is proposed:^{29, 47, 58, 59}

$$\rho_b \frac{\partial S^n}{\partial t} = \frac{\rho_b}{\theta_w} \frac{\partial S_r^n}{\partial t} + \frac{\rho_b}{\theta_w} \frac{\partial S_{nr}^n}{\partial t} = \theta_w k_{att,r}^n \Psi_r^n C^n + \theta_w k_{att,nr}^n \Psi_{nr}^n C^n - \rho_b k_{det,r}^n S^n \quad (5)$$

$$\Psi_r = \frac{S_{max,r}^n - S_r^n}{S_{max,r}^n} \quad S_{max,r} = f_r * S_{max} \quad (6)$$

$$\Psi_{nr}^i = \frac{S_{max,nr}^i - S_{nr}^i}{S_{max,nr}^i} \quad S_{max,nr}^i = (1 - f_r) * S_{max} \quad (7)$$

9 where the r and nr subscripts represent releasable and non-releasable sites, respectively, k_{att}^n is
10 the attachment rate of nanoparticle constituent i [T^{-1}], S^i is the attached phase concentration of
11 constituent i [M/M], $k_{det,r}^n$ is the detachment rate of attached phase nanoparticles from releasable
12 sites [T^{-1}], and Ψ_r and Ψ_{nr} are Langmuir-type blocking functions for each site type, described by
13 (6) and (7). The fraction of releasable sites (f_r) divides the total retention capacity into separate
14 capacities for releasable and non-releasable sites, $S_{max,r}$ and $S_{max,nr}$, respectively. This model is
15 similar to that presented in Bradford *et al.*^{29, 47} in that the releasable particles are treated
16 separately from non-releasable particles through implementation of a fraction. Herein, the two
17 sites are considered separate throughout the entire experiment, rather than only during the release
18 phase, similar to the approach of Tosco *et al.*³⁸ Consistent with other MFT-based models, as the
19 concentration of attached phase particles approaches the maximum retention capacity of a site

1 type, Ψ decreases from unity, effectively slowing down, and eventually eliminating, the kinetic
 2 attachment of suspended nanoparticles to those sites.

3 The detachment rate for releasable sites is assumed to be a step function of the aqueous
 4 salt concentration:

$$k_{det,r}^n = k_{det,r}(C^{brine}) = \begin{cases} k_{det}^0 & \text{if } C^{brine} \leq CRC \\ 0 & \text{if } C^{brine} > CRC \end{cases}$$

5 where C^{brine} is the concentration of brine in a given volume, CRC is the critical release
 6 concentration of brine, and k_{det}^0 is the detachment rate for particles in regions in which the brine
 7 concentration is below the critical release concentration. This model is similar to the Heaviside
 8 model proposed by Bradford *et al.*,^{23, 43} but allows the user to include the CRC specific to the
 9 system of interest.^{29, 47}

10 **3.3. Mathematical Model Implementation:** Implementation of the mathematical model in the
 11 SEAWAT framework was accomplished by adapting the non-equilibrium sorption reaction
 12 module in MT3DMS.⁶⁰

$$R_n = \beta \left(C^i - \frac{S^i}{K_d} \right)$$

13 where β and K_d are non-equilibrium sorption parameters required by MT3DMS. For
 14 nanoparticle attachment and release, the following functional forms were implemented for β and
 15 K_d :

$$\beta = \theta_w k_{att}^n \Psi \quad K_d = \frac{\theta_w k_{att}^n \Psi}{\rho_b k_{det}^n}$$

16 The code was modified to update these terms in space and time according to changes in attached
 17 nanoparticle mass. The two-site model described in equations (5)-(8) was implemented using
 18 two separate R_n terms, one for each class of attachment sites, r and nr . It should be noted that in

1 this implementation, k_{det} resides in the denominator of the K_d coefficient, which requires that k_{det}
2 be set to $\varepsilon = 1 \times 10^{-10}$ when the model defines it to be zero.

3 The column was simulated as a three dimensional rectangular prism, with the cross
4 sectional area equivalent to that of the experimental column (Figure S1). This simplified
5 configuration was used to reduce computational time and provided only negligible differences
6 from simulation results using a circular cross section. All outer boundaries were treated as no-
7 flow boundaries. Influent/ effluent ports were simulated by implementing a MODFLOW
8 (injection/extraction) well boundary condition at the center node in the first and last column
9 cross sections. The column inlet screen, which is designed to contain the porous media within
10 the column, also allows for influent fluid to spread across the column cross section. To mimic
11 this behavior in the model, the hydraulic conductivity of the first cross section of cells was set at
12 a value 10^3 times greater than the hydraulic conductivity of the 40-50 mesh sand.

13 **3.4 Model Parameter Estimation:** Hydrodynamic dispersion for the 40-50 mesh Ottawa sand
14 used in this study was estimated from non-reactive tracer tests in similar experiments from a
15 previous study to be $1.39 \times 10^{-2} \text{ cm}^2/\text{min}$.¹³ All parameter estimation for nanoparticle attachment
16 and detachment was conducted using a non-linear least squares optimization algorithm provided
17 by MATLAB (The Mathworks, Natick, MA).

18

19 **4. Results and Discussion**

20 **4.1 nMag Column Result:** Effluent breakthrough data for the transport of nMag-PAMPS
21 through Ottawa sand are presented in Figure 1 (experiment nMag-eff). Here, Phases 1, 2, and 3
22 represent the periods of 30 mg/L nMag suspension injection into the brine-saturated column, the
23 nMag-free brine flush of the column, and the injection of DI water through the column,

1 respectively. At the applied pore-water velocity of 3.1 m/d, nMag-PAMPS exhibited slightly
2 delayed breakthrough (ca. 1.3 PVs). Once breakthrough occurred, nMag-PAMPS reached a
3 maximum effluent concentration of 24 mg nMag/L ($C/C_0 = 0.78$) at 2.1 PV. Following the pulse
4 injection, the nMag-PAMPS concentration decreased rapidly, with approximately 46% of the
5 applied mass (ca. 918 ug) recovered in the column effluent (ca. 54% retained). Detachment
6 (release) of deposited nMag-PAMPS occurred following the introduction of DI water, with
7 measurable nMag-PAMS concentrations in the column detected approximately 1.0 PV after
8 initiation of the DI water flood. Introduction of 2.4 PVs of DI water resulted in the release of
9 approximately 21% of retained nanoparticle mass, leaving approximately 43% of the total
10 injected mass retained at the conclusion of the column experiment. In the replicate column
11 experiment, the nMag hydrodynamic diameter was measured in the influent chamber and
12 periodically in the effluent (Figure 1A). During phases 1 and 2, nMag size remained relatively
13 constant, with an average effluent hydrodynamic diameter of 56 nm, compared to 52 nm in the
14 influent. During phase 3, however, eluted nMag particles exhibited an average hydrodynamic
15 diameter of 97 nm, suggesting that released nMag particles had a greater propensity for
16 aggregation after re-entrainment or were deposited on the surface as agglomerates.
17 Representative SEM images of nMag deposited on 40-50 mesh Ottawa sand (Figure 2) reveal
18 that nMag attachment resulted in limited coverage of the sand surface, even at high loading (3.1
19 pore volumes at 1,000 mg Fe/L), and did not approach monolayer coverage. These observations
20 are consistent with the results of prior nanoparticle transport studies³⁸⁻⁴¹ and further support the
21 concept of a limited or maximum nanoparticle retention capacity (Equations 5-7). In addition,
22 calculated traditional and extended DLVO interaction energy profiles suggested that steric

1 repulsion provided only a weak attractive force between nMag and the sand surface, a result
2 which was consistent with the small amount of retention observed (Figure S4).

3 In the second column experiment (nMag-MRI), the spin-spin relaxation time (T_2), or
4 equivalently the relaxation rate, $R_2 = 1/T_2$, of the bulk fluid was measured periodically along
5 sagittal and axial planes of the column using the MRI device (Figure 3). Iron nanoparticles have
6 long been demonstrated to induce a strong shift in T_2 , even at low concentrations and under weak
7 magnetic fields, making them ideal contrast agents for a variety of applications.⁶¹ As a
8 relaxation rate, this shift is additive with respect to other contributions and proportional to
9 particle concentration for a fixed particle type and aggregation state, e.g. $R_2 = R_{2,bulk} +$
10 $k C_{nMag}$, where $R_{2,bulk}$ represents the relaxation rate of the bulk fluid in the absence of nMag
11 particles, and k represents the relaxivity, a proportionality constant which is sensitive to particle
12 aggregation state.^{32, 33} Thus, under stable aggregation conditions, magnetic nanoparticle
13 concentrations can be quantified because they are linearly correlated to R_2 . Furthermore, under
14 our experimental configuration, only pore-water suspended nMag particles are detected as
15 confirmed by the imaging measurements. Surface adhered nMag particles typically produce a
16 substantially smaller effect, because individual particles can only affect the signal from bulk
17 fluid molecules that diffuse within a region on the order of their size and surface adhesion
18 reduces this effective volume.

19 In Figure 3, the strong signal (red) indicates high R_2 , consistent with the presence of
20 suspended nMag nanoparticles in the pore water, while the weak signal (blue) indicates a low R_2
21 consistent with nMag-free brine solution. R_2 was linearly correlated to the suspended nMag
22 concentration in the pore water under constant brine conditions (Figure S2):

$$R_2 = 1.394C_{nMag} + 2.837 \quad R^2 = 0.998$$

1 Previous studies have also demonstrated that the R_2 is strongly sensitive to nanoparticle
2 aggregate size and geometry.^{32, 33, 51, 61}

$$R_2 \propto \left(\frac{n}{r_G^3}\right)^2 r_G^2$$

3 where r_G is the radius of gyration of the aggregate and n is the number of primary particles in the
4 aggregate. Because of this non-linear dependence of R_2 on nMag particle size, quantification of
5 nMag concentration from R_2 data was only possible during Phases 1 and 2 of this experiment
6 (Figure 1). Thus, R_2 profiles were primarily used to indicate presence and location of suspended
7 nMag particles during Phase 3.

8 During phase 1, nMag-PAMPS were uniformly distributed in the aqueous phase after the
9 introduction of 1.3-PVs of the influent suspension which contained ca. 30 mg/L as Fe nMag-
10 PAMPS in brine (density ca. 1.07 g/mL) (Figure 3, panels A-D). The nMag-free brine flush,
11 which was initiated in Phase 2 of the experiment, displaced suspended nMag particles from the
12 column (Figure 3, panels E-G). As noted previously, the MRI configuration did not detect
13 attached particles, and thus, the column appears completely dark blue at the conclusion of Phase
14 2 (Figure 3, panel G). At this stage of the experiment, approximately 46% of the applied nMag
15 was eluted from the column and the remaining 54% of the applied mass was deposited on the
16 quartz sand. To evaluate the release of deposited nMag, the column was then flushed with DI
17 water (Phase 3, Figure 3, panels H-I). Due the density contrast between the resident brine
18 solution (ρ_l ca. 1.07 g/mL) and the injected DI water (ρ_l ca. 0.997 g/mL), a diagonal fluid density
19 front formed within the column, resulting in flow override of lower-density DI water above the
20 more dense resident brine solution. Along this density contrast front, a strong increase in R_2

1 developed, indicating detachment and re-entrainment of nMag-PAMPS in the pore fluid (Figure
2 3, panels H-I). This behavior was attributed to the reduction in pore-water ionic strength due to
3 the DI water flood, which resulted in lower nMag-sand surface attractive forces and subsequent
4 nMag detachment. The shift in R_2 was negligible up-gradient from the angled nMag release
5 front, indicating that nMag remaining at that location within the column was still strongly
6 attached to the solid surface. In response to the DI water flood, approximately 11% of the
7 applied nMag mass was released from sand surfaces, while 43% of the applied nMag remained
8 attached. The fraction of deposited nMag mass that remained attached (ca. 80% of the total
9 deposited mass) was considered to be irreversibly attached under these experimental conditions.
10 These particles may have been strongly retained on the sand surface due to calcium ion bridging
11 across the primary energy barrier.^{17, 24, 42} In order to account for the different populations of
12 attached particles (*i.e.*, releasable and non-releasable), a two-site detachment model²⁹ was
13 employed to capture the nanoparticle release behavior observed in Phase 3. The results of nMag-
14 eff and nMag-MRI column experiments clearly demonstrate the influence of ionic strength and
15 fluid density on nanoparticle transport, retention, and release under these experimental
16 conditions.

17 **4.2 Modeling nMag Injection and Deposition:** Detachment of deposited nMag mass was
18 eligible during Phases 1 and 2 of the column experiments, as supported by the minimal R_2 signal
19 observed within the column following the passage of the nMag pulse (Figure 3), combined with
20 the absence of tailing in the effluent breakthrough curve prior to introduction of DI water (Figure
21 2A). A relatively sharp vertical displacement front was observed during Phases 1 and 2 of the
22 nMag-MRI column experiment (Figure 3) because the 30 mg/L nMag brine suspension was
23 injected into a brine-saturated column which had a similar fluid density. Based on these

1 observations, a traditional one-dimensional version of the model presented in equations (2), (5),
2 and (6) was used to determine the nMag attachment parameters.³⁹⁻⁴¹ Attachment to the
3 releasable and non-releasable sites was assumed to occur at the same rate. Based on this
4 assumption, $k_{att,r}$ and $k_{att,nr}$ were approximated as a single attachment rate, k_{att} ; likewise, $S_{max,r}$ and
5 $S_{max,nr}$ were combined into a single site, represented by the total retention capacity, $S_{max} = S_{max,r} +$
6 $S_{max,nr}$.

7 The fitted nMag breakthrough curve for Phases 1 and 2 ($k_{att}=5.28 \text{ hr}^{-1}$ and $S_{max}=5.42$
8 $\mu\text{g/g}$) is plotted with the experimental data in Figure 1A. The MFT model successfully captured
9 the nMag transport behavior, including the delayed breakthrough time (ca. 1.3 PV) and
10 magnitude, as well as the absence of breakthrough curve tailing following the passage of the
11 nMag pulse. The model-predicted solid phase retention profile following the conclusion of
12 Phase 2 is shown in Figure 1B, and indicates that the available nMag retention sites were
13 completely saturated near the column inlet, decreasing to 97% site saturation near the column
14 outlet. This retention behavior is consistent with the experimental breakthrough curve, which
15 reached a maximum relative concentration (C/C_0) of 0.8, indicating that additional solid phase
16 retention sites were still available in the column. Based on the ability of the model to capture all
17 aspects of the breakthrough curve, the assumption of a single-site attachment model was
18 considered to be appropriate for Phases 1 and 2 of the experiment. The fitted k_{att} and S_{max} were
19 then used in the multi-dimensional nanoparticle release model to simulate the entire nMag
20 column experiment (*i.e.*, Phases 1-3) discussed below.

21 **4.3 Modeling nMag Release:** In the MRI imaging results (Figure 3), the angled front observed
22 in Phase 3 was associated with both density driven flow and nanoparticle detachment, each
23 resulting from the transient brine conditions within the column. To appropriately model this

1 behavior, it was necessary to couple three-dimensional simulation of transient flow with ionic
2 strength induced nanoparticle detachment through the modified SEAWAT code. Since nMag
3 detachment behavior depends simultaneously on flow and chemistry in the experiment,
4 independent experimental determination of the detachment parameters specified in (5)-(7), k_{det}
5 and f_r , was not possible. Thus, the modified SEAWAT model was fit to Phase 3 of the measured
6 effluent breakthrough curve (Figure 1). The model results were then compared to the observed
7 R_2 profiles at consistent time points to ensure that the simulation appropriately captured the
8 observed variable density flow behavior (Figure 4).

9 Figure 4A presents the simulated centerline sagittal plane salt concentration profiles,
10 which are independent of the nanoparticle transport behavior. Comparing Figure 4A with
11 Figures 3H and 3I, it is apparent that the nMag re-entrainment front occurs along the same angle
12 as the salt concentration contours in that plane. This behavior is consistent with the hypothesis
13 that nMag detachment occurred in response to the reduction in ionic strength resulting from DI
14 water front. The nanoparticle release front was observed to occur at approximately the 45 g/L
15 salt concentration contour, and thus the critical release concentration (CRC) in subsequent
16 modeling was specified as 45 g/L.

17 Using a CRC value of 45 g/L, the two-site model (equations (5)-(7)) was fit to the Phase
18 3 effluent data (3.0 – 5.4 PV) from the nMag-eff column experiment, where f_r and k_{det} were the
19 only fitted parameters. The two-site detachment model successfully captured the measured
20 effluent concentrations from Phase 3, including the timing of the peak nMag release (ca. 4.0 PV)
21 and the slope of the subsequent tailing (Figure 1A). The predicted final nMag retention profile
22 (Figure 1B) was flat, at a constant value of 3.25 ug/g. Given that the fitted fraction of detachable
23 mass was 0.40, a comparison of the retained mass with the S_{max} value of 5.42 ug/g indicates that

1 nearly all (> 99%) of the detachable mass had been released by the end of the simulation. The
2 fitted detachment rate, k_{det} , was 2.76 hr^{-1} , a slightly slower rate than that of attachment ($k_{att} = 5.29$
3 hr^{-1}). Measured retention profiles were not available for these experiments due to the inability to
4 accurately distinguish between nMag associated iron and sand-associated iron in digested solid-
5 phase samples. However, nMag effluent concentrations at the end of the experiment decreased
6 to below $C/C_0 = 0.05$, indicating that the detachment process was essentially complete.
7 Integration of the experimental and model breakthrough curves showed that the model was able
8 to accurately capture the quantity of mass released in Phase 3, (94.1 ug simulated with 94.3 ug
9 measured). Simulation of the nMag suspended concentration profile indicated that some
10 suspended mass was still remaining in the column at the end of the simulation, mass which
11 explains the continuation of the downward slope at the end of the breakthrough curve.
12 Furthermore, although the two-site model was not able to be fit to phases 1 and 2 of the
13 experiment due to the absence of retention data, two-site model predictions of these phases using
14 parameters fitted in phase 3 suggested that the one-site model provided a reasonable estimation
15 of the retention capacity of the system (See Figure S3).

16 Comparison of sagittal R_2 profiles (Figure 3) and simulated nMag concentration profiles
17 (Figure 4) indicates that the variable density two-site detachment model was able to capture the
18 nanoparticle release behavior observed in the nMag-MRI experiment. The two-site detachment
19 model successfully captured the narrow band of nMag released along the angled injected and
20 resident fluid front as seen in the R_2 profiles. Additionally, the model was able to capture the
21 decreasing angle of the nMag front as it passed through the column. This finding suggests that
22 the angled release behavior was primarily due to the non-uniform flow patterns created by the
23 density contrast at the DI water-brine mixing front.

1 **4.4 Comparison of Nanoparticle Release Models:** To further explore the difference between
2 the two-site detachment model utilized here and more traditional one-site attachment models, an
3 additional simulation was performed. In this simulation f_r was set to 1 so that the model reduced
4 to a traditional MFT model with detachment.³⁹ This resulted in a one parameter model fit to the
5 detachment rate, k_{det} , obtained using the same fitting procedure that was employed for the two-
6 site model simulations. Comparison of the model fit to the measured effluent breakthrough
7 curve (Figure 1A) showed that the one-site model was able to capture the concentration of nMag
8 mass observed in the column effluent at the end of the experiment (ca. 5.4 PV), but was unable
9 to reproduce the concentration peak at 4.0 PV and the downward slope from 4.0 to 5.4 PV.
10 Comparison of the simulated concentration profiles (Figure 4C) to those for the two-site model
11 (Figure 4B) and the R_2 profiles (Figure 3) demonstrate that the one-site model was unable to
12 capture the absence of nMag remobilization upstream of the initial front seen in the nMag-MRI
13 experiment, despite successfully simulating the decreasing angle of the concentration front. At
14 the end of the one-site model simulation, nMag detachment continued, a result that is not
15 consistent with both the MRI results and the effluent results. The inability of the one-site model
16 to capture the behavior observed during Phase 3 further supports the use of a two-site model to
17 describe nMag release and re-entrainment in the pore fluid.

18

19 **5. Conclusions**

20 To our knowledge, this work presents the first validated mathematical model that couples
21 nanoparticle transport, deposition, and release using a variable density flow simulator. The
22 influence of transient ionic strength on nanoparticle interaction energies of aggregation and
23 deposition has been well studied and modeled,^{14, 29, 38} yet prior studies have not included the

1 potential effects of ionic strength (*i.e.*, density contrast) on simultaneous fluid flow. These
2 processes should be accounted for in systems where changes in salt or background electrolyte
3 levels are sufficient to induce nanoparticle detachment and re-entrainment in the mobile phase,
4 and when flow is altered as a result of density gradients. Relevant scenarios include the use of
5 nanoscale contrast agents for down-hole reservoir characterization, where pore-water salinity
6 may differ from that of the injected water, and nanomaterial fate and transport aquifer formations
7 that are subject to salt water intrusion.

8

9 **Acknowledgements**

10 This research was funded by the Advanced Energy Consortium (AEC) Award No. BEG08-
11 01 and BEG13-01, and the U.S. Environmental Protection Agency STAR Fellowship Program
12 (FP-917312). It has not been formally reviewed by EPA. The views expressed in this publication
13 are solely those of the authors, and EPA does not endorse any products or commercial services
14 mentioned in this publication. The authors wish to acknowledge Drs. Huiguang Zhu and Vicki L.
15 Colvin at Rice University for providing the nMag-PAMPS nanoparticles. Imaging was
16 performed at the Harvard University Center for Nanoscale Systems (CNS), a member of the
17 National Nanotechnology Infrastructure Network (NNIN), which is sponsored by the National
18 Science Foundation under Award No. ECS-0335765.

19

20 **Electronic Supplementary Information (ESI):** A schematic diagram of the nMag-MRI
21 experimental systems, description of the mathematical modeling domain, further information
22 regarding calibration of R_2 to nMag concentration in sand, comparison of one- and two-site

- 1 simulations of phases 1 and 2, DLVO interaction energy profiles for the system, and a time lapse
- 2 movie of the best fit two-site model simulation of the nMag experimental data.
- 3
- 4

1 **References**

- 2 1. T. Zhang, D. Espinosa and K. Yoon, in *Offshore Technology Conference*, Houston, TX,
3 2011.
- 4 2. H. Yu, C. Kotsmar, K. Y. Yoon, D. R. Ingram, K. Johnston, S. Bryant and C. Huh, in
5 *SPE Improved Oil Recovery Symp.*, Society of Petroleum Engineers, 2010, pp. 1-21.
- 6 3. C.-C. Hwang, L. Wang, W. Lu, G. Ruan, G. C. Kini, C. Xiang, E. L. G. Samuel, W. Shi,
7 A. T. Kan, M. S. Wong, M. B. Tomson and J. M. Tour, *Energy Environ. Sci.*, 2012, **5**,
8 8304.
- 9 4. *WO Pat.*, WO2012154332A2, 2012.
- 10 5. R. Hashemi, N. N. Nassar and P. Pereira Almaso, *Energy Fuels*, 2013, **27**, 2194-2201.
- 11 6. H. Ehtesabi, M. M. Ahadian, V. Taghikhani and M. H. Ghazanfari, *Energy Fuels*, 2014,
12 **28**, 423-430.
- 13 7. L. Hendraningrat and O. Torsæter, *Appl. Nanosci.*, 2014.
- 14 8. Q. Sun, Z. Li, S. Li, L. Jiang, J. Wang and P. Wang, *Energy Fuels*, 2014, **28**, 2384-2394.
- 15 9. J. Quinn, C. Geiger, C. Clausen, K. Brooks, C. Coon, S. O'Hara, T. Krug, D. Major, W.-
16 S. Yoon, A. Gavaskar and T. Holdsworth, *Environ. Sci. Technol.*, 2005, **39**, 1309-1318.
- 17 10. D. O'Carroll, B. Sleep, M. Krol, H. Boparai and C. Kocur, *Adv. Water Resour.*, 2013, **51**,
18 104-122.
- 19 11. D. A. Ersenkal, A. Ziylan, N. H. Ince, H. Y. Acar, M. Demirer and N. K. Coptly, *J.*
20 *Contam. Hydrol.*, 2011, **126**, 248-257.
- 21 12. T. Tosco, J. Bosch, R. Meckenstock and R. Sethi, *Environ. Sci. Technol.*, 2012, **46**, 4008-
22 4015.
- 23 13. Y. Wang, H. Zhu, M. D. Becker, J. Englehart, L. M. Abriola, V. L. Colvin and K. D.
24 Pennell, *J. Nanopart. Res.*, 2013, **15**, 1805.
- 25 14. A. R. Petosa, D. P. Jaisi, I. R. Quevedo, M. Elimelech and N. Tufenkji, *Environ. Sci.*
26 *Technol.*, 2010, **44**, 6532-6549.
- 27 15. P. C. Hiemenz and R. Rajagopalan, *Principles of Colloid and Surface Chemistry*, Third
28 Edit edn., Marcel Dekker, Inc., New York, NY, 1997.
- 29 16. M. Elimelech, J. Gregory, X. Jia and R. A. Williams, *Particle Deposition and*
30 *Aggregation: Measurement, Modelling and Simulation*, Butterworth-Heinemann,
31 Woburn, MA, 1998.
- 32 17. Y. Wang, Y. Li and K. D. Pennell, *Environ. Toxicol. Chem.*, 2008, **27**, 1860-1867.
- 33 18. N. Saleh, H.-J. Kim, T. Phenrat, K. Matyjaszewski, R. D. Tilton and G. V. Lowry,
34 *Environ. Sci. Technol.*, 2008, **42**, 3349-3355.
- 35 19. E. Pensini, B. E. Sleep, C. M. Yip and D. M. O'Carroll, *Environ. Sci. Technol.*, 2012, **46**,
36 13401-13408.
- 37 20. R. a. French, A. R. Jacobson, B. Kim, S. L. Isley, R. L. Penn and P. C. Baveye, *Environ.*
38 *Sci. Technol.*, 2009, **43**, 1354-1359.
- 39 21. I. Chowdhury, Y. Hong, R. J. Honda and S. L. Walker, *J. Colloid Interface Sci.*, 2011,
40 **360**, 548-555.
- 41 22. I. Chowdhury, D. M. Cwiertny and S. L. Walker, *Environ. Sci. Technol.*, 2012, **46**, 6968-
42 6976.
- 43 23. Y. Wang, B. Gao, V. L. Morales, Y. Tian, L. Wu, J. Gao, W. Bai and L. Yang, *J.*
44 *Nanopart. Res.*, 2012, **14**.

- 1 24. Y. Liang, S. A. Bradford, J. Simunek, H. Vereecken and E. Klumpp, *Water Res.*, 2013,
2 **47**, 2572-2582.
- 3 25. I. R. Quevedo and N. Tufenkji, *Environ. Sci. Technol.*, 2009, **43**, 3176-3182.
- 4 26. S.-W. Jeong and S.-D. Kim, *J. Environ. Monit.*, 2009, **11**, 1595-1600.
- 5 27. Z. Li, E. Sahle-Demessie, A. A. Hassan and G. a. Sorial, *Water Res.*, 2011, **45**, 4409-
6 4418.
- 7 28. A. R. Petosa, S. J. Brennan, F. Rajput and N. Tufenkji, *Water Res.*, 2012, **46**, 1273-1285.
- 8 29. S. Torkzaban, S. a. Bradford, J. Wan, T. K. Tokunaga and A. Massoudieh, *Environ. Sci.*
9 *Technol.*, 2013, **47**, 11528-11536.
- 10 30. A. M. El Badawy, T. P. Luxton, R. G. Silva, K. G. Scheckel, M. T. Suidan and T. M.
11 Tolaymat, *Environ. Sci. Technol.*, 2010, **44**, 1260-1266.
- 12 31. C. T. Simmons, T. R. Fenstemaker and J. M. Sharp, *J. Contam. Hydrol.*, 2001, **52**, 245-
13 275.
- 14 32. Y. C. Park, J. Paulsen, R. J. Nap, R. D. Whitaker, V. Mathiyazhagan, Y.-Q. Song, M.
15 Hürlimann, I. Szleifer and J. Y. Wong, *Langmuir*, 2014, **30**, 784-792.
- 16 33. Y. Park, R. D. Whitaker, R. J. Nap, J. L. Paulsen, V. Mathiyazhagan, L. H. Doerrer, Y.-
17 Q. Song, M. D. Hürlimann, I. Szleifer and J. Y. Wong, *Langmuir*, 2012, **28**, 6246-6255.
- 18 34. H. G. Bagaria, Z. Xue, B. M. Neilson, A. J. Worthen, K. Y. Yoon, S. Nayak, V. Cheng, J.
19 H. Lee, C. W. Bielawski and K. P. Johnston, *ACS Appl. Mater. Interfaces*, 2013, **5**, 3329-
20 3339.
- 21 35. K. Y. Yoon, Z. Li, B. M. Neilson, W. Lee, C. Huh, S. L. Bryant, C. W. Bielawski and K.
22 P. Johnston, *Macromolecules*, 2012, **45**, 5157-5166.
- 23 36. K. Y. Yoon, C. Kotsmar, D. R. Ingram, C. Huh, S. L. Bryant, T. E. Milner and K. P.
24 Johnston, *Langmuir*, 2011, **27**, 10962-10969.
- 25 37. K.-M. Yao, M. T. Habibiyan and C. R. O'Melia, *Environ. Sci. Technol.*, 1971, **5**, 1105-
26 1112.
- 27 38. T. Tosco, A. Tiraferri and R. Sethi, *Environ. Sci. Technol.*, 2009, **43**, 4425-4431.
- 28 39. Y. G. Wang, Y. S. Li, J. D. Fortner, J. B. Hughes, L. M. Abriola and K. D. Pennell,
29 *Environ. Sci. Technol.*, 2008, **42**, 3588-3594.
- 30 40. Y. S. Li, Y. G. Wang, K. D. Pennell and L. M. Abriola, *Environ. Sci. Technol.*, 2008, **42**,
31 7174-7180.
- 32 41. S. Torkzaban, Y. Kim, M. Mulvihill, J. Wan and T. K. Tokunaga, *J. Contam. Hydrol.*,
33 2010, **118**, 208-217.
- 34 42. S. Torkzaban, J. Wan, T. K. Tokunaga and S. a. Bradford, *J. Contam. Hydrol.*, 2012,
35 **136-137**, 86-95.
- 36 43. Y. Liang, S. a. Bradford, J. Simunek, M. Heggen, H. Vereecken and E. Klumpp, *Environ.*
37 *Sci. Technol.*, 2013, **47**, 12229-12237.
- 38 44. J. Bergendahl and D. Grasso, *AIChE J.*, 1999, **45**, 475-484.
- 39 45. J. Bergendahl, *Chem. Eng. Sci.*, 2000, **55**, 1523-1532.
- 40 46. S. Torkzaban, H. N. Kim, J. Simunek and S. a. Bradford, *Environmental science &*
41 *technology*, 2010, **44**, 1662-1669.
- 42 47. S. A. Bradford, S. Torkzaban, H. Kim and J. Simunek, *Water Resour. Res.*, 2012, **48**,
43 W09509.
- 44 48. J. L. Paulsen, M. H. Donaldson, S. S. Betancourt and Y.-Q. Song, *J. Magn. Reson.*, 2011,
45 **212**, 133-138.

- 1 49. Y. Wang, M. D. Becker, V. L. Colvin, K. D. Pennell and L. M. Abriola, *Environ. Sci.*
2 *Technol.*, 2014, **Submitted**.
- 3 50. P. T. Callaghan, *Principles of Nuclear Magnetic Resonance Microscopy*, Clarendon
4 Press, Oxford, 1991.
- 5 51. K. A. Brown, C. C. Vassiliou, D. Issadore, J. Berezovsky, M. J. Cima and R. M.
6 Westervelt, *J. Magn. Magn. Mater.*, 2010, **322**, 3122-3126.
- 7 52. C. D. Langevin, D. T. Thorne Jr., A. M. Dausman, M. C. Sukop and W. Guo, *SEAWAT*
8 *Version 4: A Computer Program for Simulation of Multi-Species Solute and Heat*
9 *Transport*, U.S. Geological Survey, Reston, Virginia, 2008.
- 10 53. J. Bear, *Dynamics of Fluids in Porous Media*, Elsevier Publishing Ccompany, Inc., New
11 York, NY, 1972.
- 12 54. C. Zheng and P. P. Wang, 1999, p. 220.
- 13 55. A. W. Harbaugh, E. R. Banta, M. C. Hill and M. G. Mcdonald, *MODFLOW-2000, The*
14 *U.S. Geological Survey Modular Ground-Water Model - User guide to modularization*
15 *concepts and the ground-water flow process*, U.S. Geological Survey, 2000.
- 16 56. D. Thorne, C. D. Langevin and M. C. Sukop, *Comput. Geosci.*, 2006, **32**, 1758-1768.
- 17 57. R. R. Goswami and T. P. Clement, *Water Resour. Res.*, 2007, **43**, W04418.
- 18 58. J. F. Schijven and S. M. Hassanizadeh, *Critical Reviews in Environmental Science and*
19 *Technology*, 2000, **30**, 49-127.
- 20 59. J. F. Schijven, S. M. Hassanizadeh and R. H. a. M. de Bruin, *J. Contam. Hydrol.*, 2002,
21 **57**, 259-279.
- 22 60. C. Bai and Y. Li, *J. Contam. Hydrol.*, 2012, **136-137**, 43-55.
- 23 61. I. Koh and L. Josephson, *Sensors (Basel)*, 2009, **9**, 8130-8145.
- 24
- 25

1 **Table 1.** Experimental and model parameters for the column experiments.

Experimental Values		
Parameter	Value	Units
D^a	2.55	cm
L^b	10.7	cm
d_{50}^c	3.55E-01	mm
θ_w^d	3.67E-01	-
Q^e	4.00E-01	mL/min
v_p^f	2.13E-01	cm/min
D_h^g	1.39E-02	cm ² /min
PW - Phase 1 ^h	1.3	PV
PW - Phase 2 ⁱ	1.5	PV
PW - Phase 3 ^j	2.6	PV
$C_0 - nMag^k$	32.6	mg/L
$C_0 - Salt^l$	100	g/L
Ret^m	43	%
ρ_{DI}^n	0.997	g/mL
ρ_{Brine}^p	1.07	g/mL

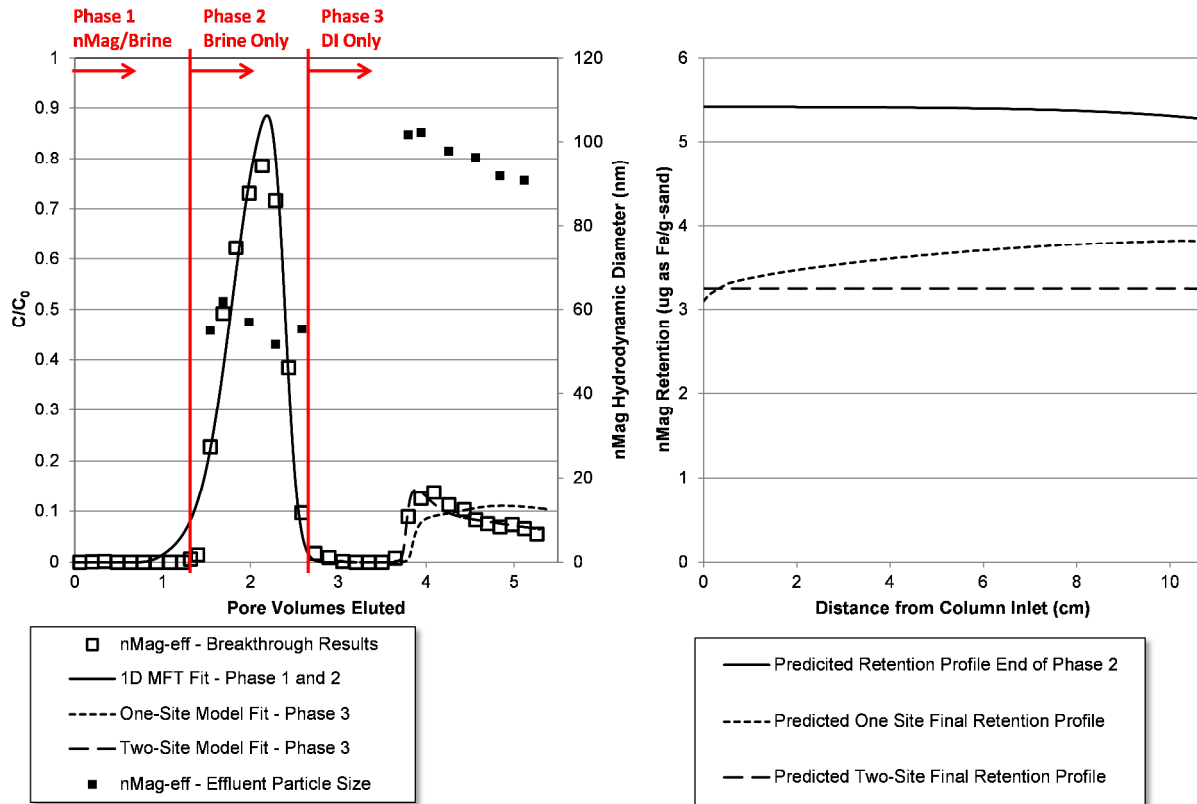
Superscripts: a – column diameter; b – column length; c – mean sand grain size; d – volumetric water content; e – Flow rate; f – pore water velocity; g – hydrodynamic dispersion; h,i,j – pulse widths for each phase; k,l – initial concentrations for each constituent; m – percent retention; n – DI water density; p – Brine density.

Modeling Values		
Parameter	Value	Units
β_c^a	7.32E-04	L/g
$k_{att,nr}^b$	8.80E-02	min ⁻¹
$k_{att,r}^c$	8.80E-02	min ⁻¹
S_{max}^d	5.42	ug/g
f_r^e	0.40	-
$k_{det,r}^f$	4.60E-02	min ⁻¹
CRC	45	g/L

Superscripts: a – Volumetric expansion coefficient for salt concentration; b – attachment rate for non-releasable sites; c – attachment rate for releasable sites; d – total solid phase retention capacity; e – fraction of releasable sites; f – detachment rate for releasable sites.

2

1

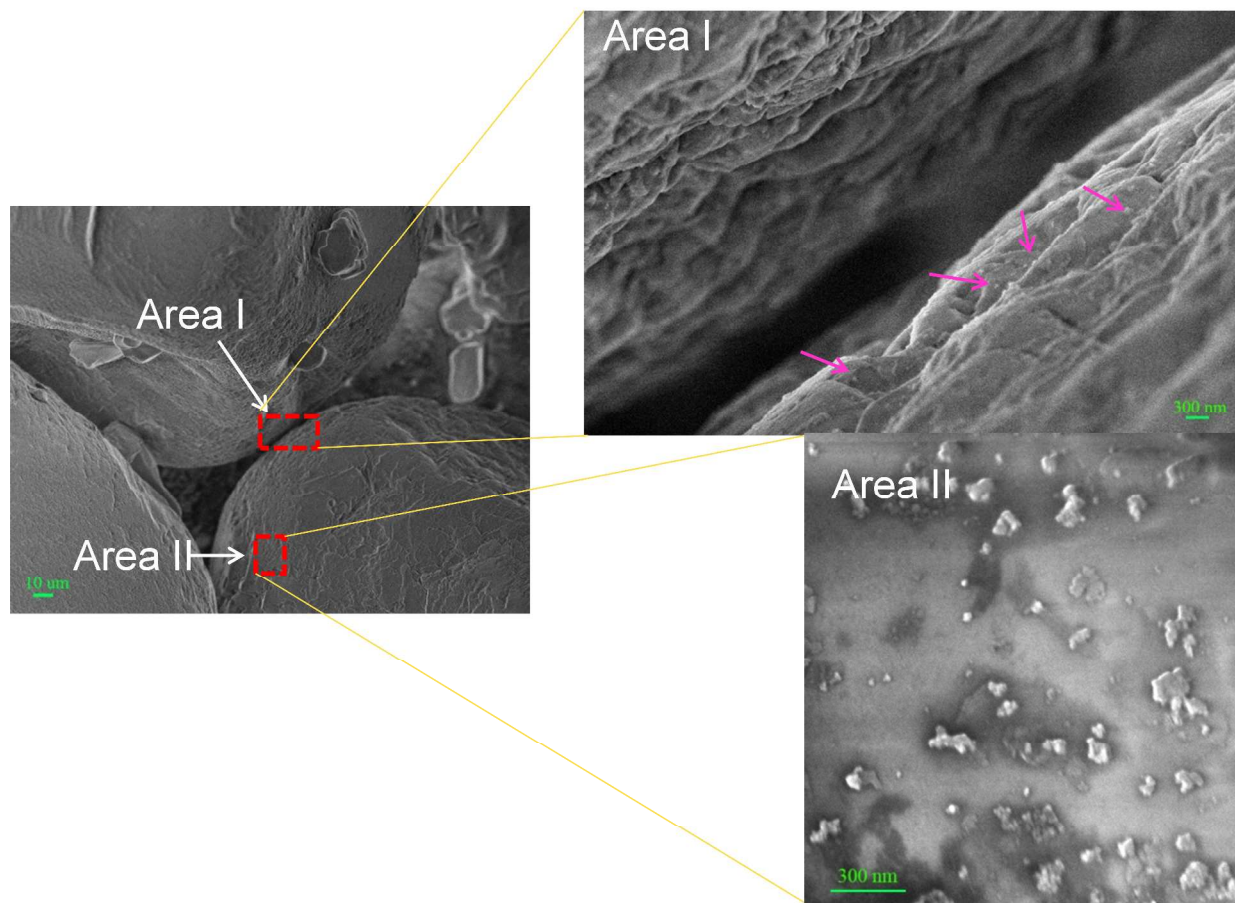


2

3 **Fig. 1:** Effluent nMag breakthrough curves and simulated retention profiles. On the
 4 breakthrough curve, simulation results are shown from the 1D model for phases 1 and 2 and
 5 from the multi-dimensional model for phase 3. Breakthrough results in phase 3 are from the
 6 one- and two-site release models. On the retention curve, predicted retention profiles are shown
 7 at the end of phase 2, and the end of phase 3 for one- and two-site release models.

8

1

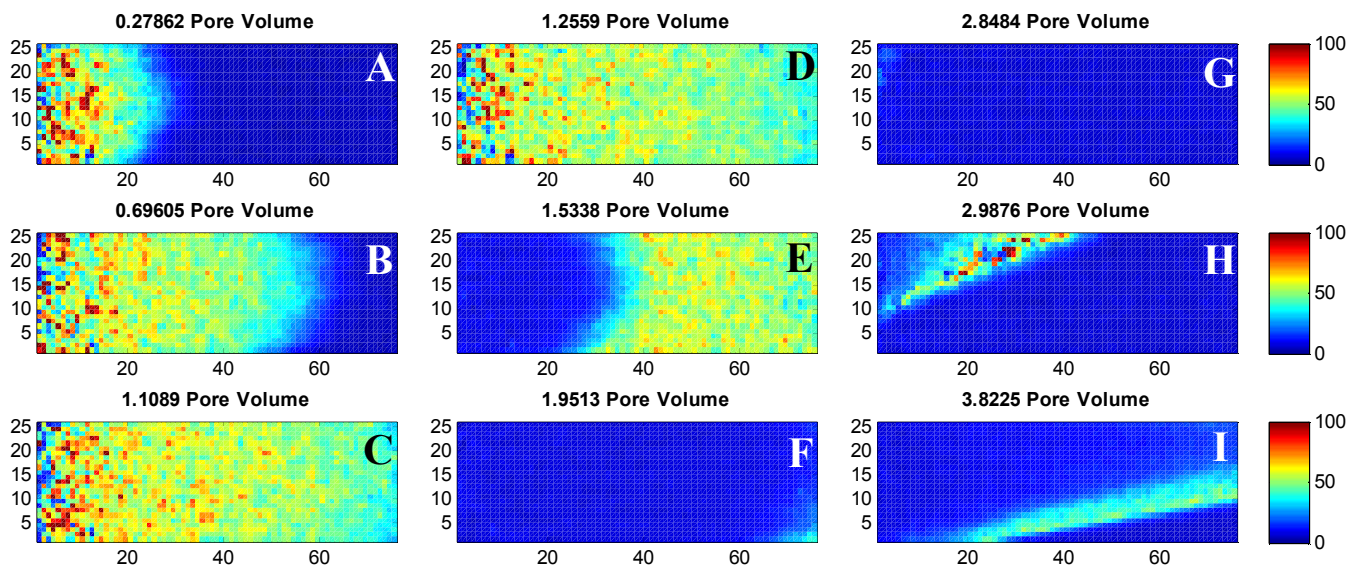


2

3

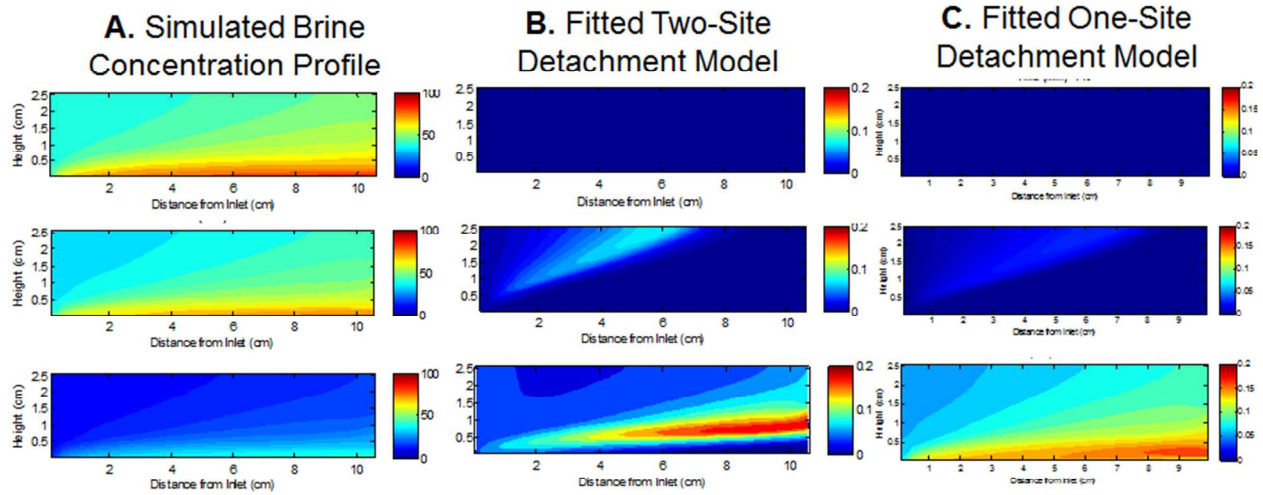
4 **Fig. 2:** SEM Images of nMag nanoparticles deposited on the surface of 40-50 mesh Ottawa Sand
5 from a representative column experiment following a 3.1 PV injection of 1000 mg/L nMag
6 suspension.

7



1 **Fig. 3:** Time series of measured relaxation rate (R_2) along the sagittal plane of the imaged
 2 column. The first column presents the nMag injection phase (Phase 1), the second presents the
 3 brine flush phase (Phase 2), and the third presents the DI flush phase (Phase 3). Horizontal and
 4 vertical axes correspond to length in millimeters.

5



1

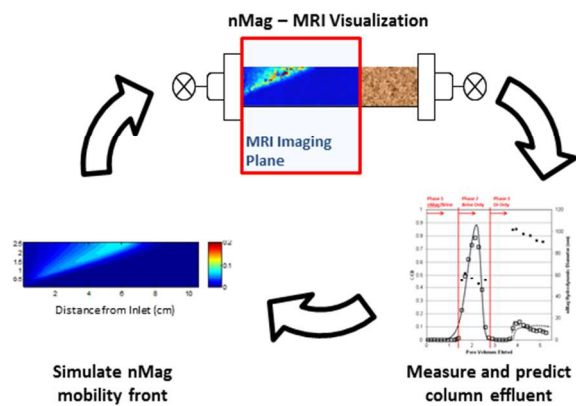
2 **Fig. 4:** Comparison of fitted model result to MRI images at the three time points from Figure 3

3 following initialization of DI injection (Phase 3). Column A presents corresponding salt

4 concentration profiles, Column B presents the two-site model best fit, and column C presents the

5 one-site model best fit.

6



- 1
- 2 **Text for graphical abstract.** In situ imaging and mathematical modeling capture the effects of
- 3 salinity changes on magnetite (Fe_3O_4) nanoparticles deposition and transport in porous media.